View metadata, citation and similar papers at core.ac.uk
brought to you by CORE
provided by CURVE/open

Evolution of a laser shock peened residual stress field locally with foreign object damage and subsequent fatigue crack growth

Zabeen, S. , Preuss, M. and Withers, P. J.

Author post-print (accepted) deposited in CURVE February 2016

Original citation & hyperlink:
Zabeen, S. , Preuss, M. and Withers, P. J. (2014) Evolution of a laser shock peened residual stress field locally with foreign object damage and subsequent fatigue crack growth. Acta Materialia, volume 83 : 216-226
http://dx.doi.org/10.1016/j.actamat.2014.09.032

DOI 10.1016/j.actamat.2014.09.032
ISSN 1359-6454

Copyright © and Moral Rights are retained by the author(s) and/ or other copyright owners. A copy can be downloaded for personal non-commercial research or study, without prior permission or charge. This item cannot be reproduced or quoted extensively from without first obtaining permission in writing from the copyright holder(s). The content must not be changed in any way or sold commercially in any format or medium without the formal permission of the copyright holders.

This document is the author's post-print version, incorporating any revisions agreed during the peer-review process. Some differences between the published version and this version may remain and you are advised to consult the published version if you wish to cite from it.

CURVE is the Institutional Repository for Coventry University

S. Zabeen, M. Preuss, P.J. Withers, Evolution of a laser shock peened residual stress field locally with foreign object damage and subsequent fatigue crack growth, Acta Materialia. 83 (2015) 216-226.

Evolution of a laser shock peened residual stress field locally with foreign object damage and subsequent fatigue crack growth

S. Zabeen[1], M. Preuss[2], and P.J. Withers[2]

[1] Materials Engineering, Walton Hall, The Open university, Milton Keynes, MK7 6AA [2.] School of Materials, University of Manchester, Grosvenor St., Manchester M13 9PL, United Kingdom

Email: Philip.withers@manchester.ac.uk

Abstract

Foreign object damage (FOD) can seriously shorten the fatigue lives of components. On the other hand, laser shock peening improves fatigue life by introducing deep compressive residual stress into components. In this paper we examine how the non-uniform steep residual stress profile arising from FOD of laser peened aerofoil leading edges vary as a function of fatigue crack growth under high cycle fatigue and mixed high (HCF) and low (LCF) cycle fatigue conditions. The ballistic FOD impacts were introduced by impacting a cube edge at an angle of head-on (0 degrees) to the leading edge. The residual stress distributions have been mapped by synchrotron X-ray diffraction prior to cracking and subsequent to short (~1 mm) and long (up to 6 mm) crack growth.

The results suggest that the local residual stress field is highly stable even to the growth of relatively long cracks.

1 Introduction

Laser shock peening (LSP) induced compressive residual stresses have been found to affect the fatigue crack growth behaviour by delaying the crack initiation and by decelerating the crack propagation rate for aluminium alloys [1-4], and also for Ti-6Al-4V [5-8]. For thick Ti-6Al-4V components, the residual stresses introduced by laser peening are typically ~600 MPa near surface, and reduce linearly to a depth of around 2 mm whereupon balancing tensile stresses are encountered [9]. For thin (a few mm thick) aerofoil specimens, the compressive stresses typically extend through thickness provided there is sufficient material to restrain the lateral expansion of the peened region [10, 11]. LSP is used to enhance material lifetimes predominantly under fatigue related conditions although benefits have also been seen under other damage modes such as galling, stress corrosion cracking, corrosion, wear and fretting fatigue [9, 12]. The stability of the residual stress field has been investigated by a number of researchers for shot peened steel [13-17], nickel base superalloys [18-20], and titanium alloys [21]. However, the relaxation of LSP'd residual stress has not been extensively studied to date although resistance to fretting has been quantified [9]. The residual stress state and their stability for different materials is summarised in [22, 23]

In the aerospace industry, foreign object damage (FOD) is one of the major life-limiting factors that can markedly reduce the fatigue life of aeroengine components. A small (<3 mm in depth) FOD notch may reduce fatigue life by over 50% [6]. The effect is a complex one. Hall et al. [24] have found that fatigue cracks initiate much faster under LCF, HCF and LCF+HCF from cube edge impact FOD notches that have been stress relieved relative to those that have not, suggesting that the compressive residual stresses at the notch tip [25] may be beneficial. Conversely, Thompson et al. [26] using spherical indents found that stress relief improves the fatigue limit stress invoking tensile stresses at the edge of the crater rim (near where the cracks initiate) [27]. Indeed, LSP has been found to improve the fatigue resistance of Ti-6Al-4V [6] in the presence of FOD, at low stress ratios (R=0.1). However, no improvement has been observed at higher stress ratios (R=0.8). Hammersley et al., [28] also observed similar results.

From published fatigue test results, it is easily understood that the deep compressive residual stresses introduced by LSP treatment causes the observed improvement. In order to incorporate any associated fatigue life benefit arising from LSP into damage tolerant design, it is important to be able to quantify these residual stresses and their evolution through life accurately. There have been a handful of research studies where residual stresses have been mapped post FOD [25, 27] These tend to show a compressive stress immediately below the notch with tensile stresses located at greater depth below the notch and near the edge of the crater. This broad pattern seems to occur irrespective of the impactor geometry, although the actual levels of stress vary. The effect of FOD impact on laser peened specimens has also been examined for both head on (0°) and 45° simulated impacts[11, 29]. Local to edge-on cube impact the residual stress is characterised by a peak compressive stress parallel to the leading edge immediately below the notch. Comparison of the stress fields introduced by leading edge FOD with [11, 29] and without [25] prior LSP under similar conditions indicate that the stresses introduced at the notch tip are surprisingly similar. The effects of the prior laser peening are seen some distance further from the notch tip: both the tensile region around the crater and, most importantly, the tensile region lying some distance below the notch tip have been removed. This may explain the increase in fatigue life for impact damaged specimens for which the crack propagates from the notch tip.

In view of the potentially beneficial effects of the residual stresses arising from the FOD impact immediately below the notch and those introduced by laser peening somewhat further below the notch tip, it is critical to quantify their stability and redistribution during fatigue crack growth. Aero-engine rotating components such as fans and blades are generally subjected to high frequency vibratory loading (HCF), which is superimposed onto low frequency centrifugal loading (often at high stress). Consequently, in this paper the redistribution of the residual stresses have been quantified as a function of fatigue cycling and crack growth both for LCF and combined cycle (LCF+HCF) fatigue cycling prior, and subsequent, to short (<1 mm) and long (up to 6 mm) levels of crack growth.

2 Materials and Experimental Method

2.1 Material

Ti-6Al-4V is widely used for compressor blades and is thus studied here. The manufacturing process involves forging the material above and below the β transus to break up the coarse lamellar microstructure. Subsequently, the alloy was solution treated at about 927 °C (below the β-transus) followed by a stress relief heat treatment at 705 °C for 2 hours. This thermomechanical processing route produced a bimodal microstructure comprising ~60% primary α and 40% (by volume) lamellar colonies (see Figure 1). The room temperature mechanical properties of Ti-6Al-4V can be represented by Young's modulus, E=103 GPa, Poisson's ratio, υ=0.3, yield strength, σ_Y = 860MPa and an ultimate tensile strength, σ_{UTS} = 980MPa [30]. Specimens were machined from the forged blocks to form a generic leading edge profile, as shown in Figure 2.

2.2 LSP treatment

The specimens were laser shock peened over the leading edge using parameters that provided an optimum balance between induced residual stresses (FOD tolerance) and acceptable distortion of the leading edge profile. This was carried out by the Metal Improvement Company, USA at a power density of 10 GW/cm^2, using a square spot (size 3 x 3 mm^2), 50% overlap and 200% coverage, with a pulse duration of 27 ns. The LSP'd region extends 6 mm from the leading edge and over 65 mm along it (Figure 2a).

2.3 Simulated FOD

To simulate the FOD damage that occurs as a result of ingested particles at high velocities and strain rates, the specimens were impacted ballistically using a 12 mm bore light compressed gas gun at the Department of Engineering Science, Oxford University, UK. The gas gun was equipped with a 2 litre gas cylinder connected to a 2.5 m long sleeved barrel. Details of the damage simulation technique are described elsewhere [31]. To replicate the 'worst case' damage, hardened steel cubes were chosen having a hardness value between Rockwell C 62 and 64. The steel cube was mounted in a nylon sabot to prevent rotation and to ensure that the steel cubes hit the leading edge in a controlled manner. Each sample was mounted in a cross-vice that could be rotated and translated using a motor-driven system with micrometre precision. A 3.2 mm hardened steel cube was directed at an angle of 0° to the leading edge (parallel to the transverse 'x' direction) with an impact velocity of 200 m/s. In this case, the cube hit the specimen edge first (Figure 2b). The notch depth for each specimen was measured by an optical microscope from a profile view of the notch.

2.4 Specimen Studied

The specimens were fatigued by Spanrad and Tong at Portsmouth University as described in [32] under 4-point bend and constant amplitude cyclic loading using a servohydraulic twin actuator 100kN testing machine. The support span was 107 mm and the loading span was 57 mm. In order to represent conditions appropriate for aeroengines, LCF and combined (HCF+LCF) cycle fatigue were studied (Figure 3). HCF was conducted at a frequency of 80 Hz and a load ratio of

R = 0.7; whilst low cycle fatigue was conducted at 0.25 Hz at a load ratio of R = 0.1. Each combined cycle (CCF) block comprised 1000 HCF fatigue cycles and 1 LCF cycle. The direct current potential drop (DCPD) method was used to monitor crack initiation and growth to ~10μm resolution. The corresponding fatigue loading conditions are summarised in Table 1.

2.5 High Energy Synchrotron X-ray Diffraction

The residual stress field has been tracked for a set of specimens (see Table 1) as a function of the number of LCF or CCF cycles. In order to do this it was necessary to aggregate the results over multiple experimental periods allocated on different diffractometers capable of residual strain analysis to allow the specimens to be returned periodically to the mechanical testing laboratory at Portsmouth for further cycling. The set-ups at the different beamlines are summarised in table 2. Great care was taken to ensure that the residual strains are directly comparable between the different international facilities; it is likely that the diffraction peak widths are less comparable between sources.

APS (1-ID-C): Measurement was carried out in transmission geometry where the specimens were placed perpendicular to the incoming monochromatic X-ray beam (energy 65 keV). Complete Debye-Scherrer rings were acquired for each location on a MAR-345 image plate detector. Further details of the experimental set up and data processing can be found elsewhere [33].

HASYLAB (HARWI-II): Similar set up to the APS except that the beam energy was 65 keV and a MAR 555 detector was used to collect the Debye-Scherrer rings.

PETRA-III (HEMS): The high energy material science (HEMS) beamline PO7 was used at an energy of 53.3 keV with the diffracted Debye-Scherrer cones captured by a MAR-345 image plate detector.

ESRF (ID31): Here the measurements were carried out in depth resolved transmission geometry. A monochromatic synchrotron X-ray beam was selected (50.8keV, 0.244Å) by a Si (111) double crystal monochromator. To define the gauge volume, two slits were used on the incident and diffracted beam resulting in an elongated gauge volume that was 0.9 mm long, 0.4 mm wide and 0.05 high. The diffracted beam was passed through an analyser crystal and recorded on the central detector of the 9-channel multi-analyser stage. The use of the analyser crystal is advised for near surface measurements [34] to minimise peak shifts due to incomplete gauge volume leading to pseudo strains [35].

Data Analysis

The resulting diffraction peaks were fitted to Gaussian (Pseudo-Voigt for ID31) functions and the d-spacing inferred using Bragg's equation. In all cases single peak analysis was carried out using the $(10\bar{1}2)$ diffraction peak from the Ti-α phase. Although the $(10\bar{1}2)$ peak has a much lower intensity than $(10\bar{1}1)$ peak it was chosen because it displays low intergranular strain [36], and hence is representative of the macrostress. Elastic strain was obtained in the usual manner relative to a strain-free lattice spacing, d_0. This was obtained using the far-field approach [37] from a few measurement points located 55 mm away from the notch centre either side of the sample, and also from a small strain-free reference sample. Measurements were taken at five locations within the sample and averaged to obtain a single value of d_0. The strains (ε) in the directions longitudinal (y) and transverse (x) to the leading edge (see Figure 2a) were used to infer the stresses (σ) assuming a bi-axial stress state (σ_{zz}=0):

$$\sigma_{xx} = \frac{E}{1-\upsilon^2}\left(\varepsilon_{xx} + \upsilon\varepsilon_{yy}\right) \quad \textbf{\textit{and}} \quad \sigma_{yy} = \frac{E}{1-\upsilon^2}\left(\varepsilon_{yy} + \upsilon\varepsilon_{xx}\right) \qquad \textbf{\textit{Equation 1}}$$

Where, the elastic constants are given in section 2.1.

3 Results

3.1 Shakedown of residual stresses prior to fatigue crack initiation

Figure 4 shows the 2D residual stress field prior to, and following, a single block (N=1) of combined LCF and HCF loading (see Table 1). The experimental and systemic error in the residual stress results presented in this study lies within ± 20 MPa. The notch in sample S-2 (mapped after 1 cycle) is marginally deeper (by 0.06 mm) than that in sample S-1 (as-FOD'd condition) due to the variability of the FOD impact process which may explain the slightly larger compressive strain field at the bottom of the notch for specimen S-2. Either way, the maps and the line profiles in Figure 5 suggest negligible relaxation after a single block (N=1) with σ_{max} = 0.50 σ_y. This compares with the observations by Boyce et al. [38] who did observe some relaxation under LCF at 0.54 σ_y (R=0.1 and N=1 cycle) but not at 0.35 σ_y.

A similar picture of negligible relaxation emerges after N = 100 blocks of combined cycle fatigue (Figure 5). This suggests that LSP induced residual stresses are highly stable to tensile fatigue loading at least prior to crack growth. This agrees well with the results published by Nalla et al [5] where only a 20% stress relaxation has been reported after applying half number of cycles of the total cycles to failure ($N=0.5N_f$) at a stress amplitude of $\sigma_a = 0.7\sigma_y$ under complete reverse bending.

3.2 Effect of Crack Growth on residual stress under LCF

In order to quantify the extent of stress relaxation as a function of crack growth two specimens were progressively cracked under LCF (S-5 and S-6 – see Table 1). In both cases the crack grew from the notch tip as illustrated in Fig 6 for S-6.

It is clear from Figure 7 that despite the presence of a fatigue crack grown under a significant load each cycle ($S_{max} = 0.68\,\sigma_y$) the characteristic LSP+FOD residual strain field remains. Even in the case where the crack has grown over 5 mm a compressive field near the notch remains. Only much further from the notch, where the original residual stress field becomes tensile, does the crack affect significantly the stress distribution. The line profiles in Figure 8 (in stress) confirm the similarity of the strain field after 0.5mm of crack growth to the stress field prior to LCF. While the presence of the 5.3 mm long crack has brought about some degree of re-equilibration, most notably a reduction of the compressive stress beneath the notch and the loss of tensile strain beyond the peened region (peened to 6 mm from LE), the field is now compressive along the whole length of the crack. This will act to hold the crack faces shut over a significant fraction of the fatigue cycle.

3.2.1 Effect of Crack Growth on residual stress under CCF

Cracks were grown in two specimens under combined cycle fatigue (S-3 and S-2 – see Table 1) allowing the changes taking place as a function of crack length to be determined. For each sample, a crack formed at the notch tip, though the crack paths were not straight (see Figure 9) for specimens S-2 and S-3.

Similar to what was found for the LCF cycling, very little redistribution of the residual stress field occurs either for Δa = 1 mm or Δa = 2.1 mm as exemplified by the plots in Figure 10. Closer examination of the line profiles in Figure 11 (in stress) confirms that very little stress redistribution has occurred. It can be observed that after Δa=2.1mm the residual stress map has become asymmetric. This can be understood from the SEM micrograph of the crack shown in Figure 9b, which shows the crack to have deviated from the mid-line (y=0).

3.3 Stress redistribution after an overload

It is apparent from the above results that LSP'd residual stresses are highly stable to fatigue crack growth. A specimen was overloaded up to the yield stress of the material (S_{max} = 860 MPa), which is twice as large as the load used for CCF. This sequence introduced a crack of 2.2 mm in length (Figure 12b). The resulting residual strain distribution (in the longitudinal direction) is presented in Figure 12a. It is clear by comparison with Figure 4 that the peak compressive stress has decreased by around 35% although the associated local plasticity has meant that it has broadened in extent.

4 Discussion

The stability of the residual stress on cyclic loading depends on the initial residual stress and its gradient, type of loading, mean loading, and cyclic deformation behaviour of the material etc.

A striking feature that has been found in this study is the stability of the residual stress distribution even for relatively long cracks. Only when the crack had penetrated the original tensile zone beyond the laser-peened region a significant redistribution in stress was observed due to the inability of a crack to sustain a tensile stress across it. Of course, this implies that the crack faces are under compression for a large portion of the fatigue cycle throughout the crack growth process, which is important information from a structural integrity assessment viewpoint because it means that the residual stresses can significantly slow the progress even of quite long cracks [39]. Further, this suggests that the extent of plastic deformation caused by the crack is very localised and unable to significantly remove the eigenstrains (misfits) that are responsible for the original residual stress.

Given that a diffraction peak is generally broadened by plastic deformation, the variation in the peak full width at half maximum (FWHM) across the fracture surfaces has been used previously to assess the plastic zone and thereby the stress intensity experienced at the crack tip [40]. Withers [41] has shown that synchrotron x-ray diffraction measurements within steep stress gradients can result in significant peak broadening that might be misinterpreted as a result of plasticity. Nevertheless, it is helpful to compare the FWHM profiles for the different cases in Figure 13. While the absolute FWHM values are not comparable from beamline to beamline, the broad distributions can be compared usefully. From this it is clear that the passage of the crack has had an effect on the FWHM for the CCF and LCF cases only very close to the crack, although for the latter the breadth of the affected region extends some 0.5 mm or so from the location of the crack plane. By contrast, a much more significant plastically affected zone (~2.2 mm) is observed local to the crack for the overloaded sample confirming a much more extensive plastically affected area in this case (see Figure 12 d).

A detailed analysis of the crack-tip mechanics and the determination of the stress state at the crack-tip are beyond the scope of this study. However, an estimation of the plastic zone size can help illuminate the observations. Under a monotonic load, the width of the forward plastic zone r_p can be estimated using [42].

$$\boldsymbol{r_p = \frac{1}{\pi}\left(\frac{K_{max}^{eff}}{\sigma_y}\right)^2} \qquad \textbf{\textit{Equation 2}}$$

where K_{max}^{eff} is the effective maximum applied stress intensity factor. In the case of cyclic loading the reverse plastic zone size (PZS), Δr_{p} can be expressed:

$$\Delta r_p = \tfrac{1}{4}\, r_p \qquad \textbf{\textit{Equation 3}}$$

This approach provides an estimate of the plastic zone ahead of the crack-tip where no RS is present in the body. Where residual stresses are present such as in LSP+FOD'd specimens, so-called 'crack closure' can occur. We call this residual stress induced crack closure, and it causes the actual stress intensity range ΔK^{eff} to be reduced from the theoretical ΔK that would be found if the crack were open at all times during a load cycle. For a crack in a residual stress field that generates a stress intensity contribution K_{res}, the effective maximum and minimum stress intensities would be expected to be K_{max}+K_{res} and K_{min}+K_{res} respectively giving ΔK^{eff} = K_{max}-K_{min}. If however $K_{min}+K_{res}<0$ then ΔK^{eff} becomes (K_{max} + K_{res}).

The reverse plastic zone for an advancing fatigue crack in a residual stress field is given by McClung [43]:

$$\Delta r_p' = \frac{1}{\pi}\left(\frac{\Delta K_{eff}}{2\sigma_y + (\sigma_{cl} - \sigma_{\min})}\right)^2 \qquad \textbf{\textit{Equation 4}}$$

Where; σ_{cl} is the stress at the unloading cycle at which the crack faces first closes and σ_{min} is the minimum stress in the cycle. In this study the 'crack-closure' stress, σ_{cl} was not explicitly measured. Nevertheless, Equation 4 is still valid with the assumption of σ_{cl} - σ_{min} = 0 where crack closure occurs at the minimum applied load, to estimate the maximum size of the plastically deformed zone ahead of the crack tip.

The variation of K_{max}^{eff} as a function of crack length for the generic LE geometry is shown in Figure 14a for σ_{max} = 435 MPa under LCF and CCF loading conditions. In the same figure, the variation of stress intensity factor due to residual stress K_{res}, with crack length is also plotted. From this the corresponding forward plastic zone has been calculated using Equation 3 and compared with that for the unpeened condition to provide an estimate of the upper bound of the deformation zone size.

The corresponding forward and reverse PZS (using Equation 4) for the peened specimens are presented in Figure 14b. The high compressive residual stresses result in a marked reduction in K_{max}^{eff} and thus the PZS. The maximum size of the reverse plastic zone is approximately 100 μm at the beginning of the crack growth, which then decreases with increasing crack length. Since the superposition principle was used to determine K_{res}, and hence the effective stress intensity factor range, the shape of the PZS profiles directly reflect the shape of corresponding residual stress profile. Here the grain size of the Ti-α phase is about 25 μm and the PZS is about 4 times this size. Consequently only a few grains around the crack tip are plastically affected.

For higher applied stress one might expect a larger plastic zone size. In this case we would expect a plastic zone size of 100 μm. This is smaller than that +/-1 mm extent of the FWHM variation away from the crack plane evident in Figure 13d.

5 Conclusions

Laser shock peening introduces through-thickness compressive residual stresses in Ti-6Al-4V thin aerofoil sample up to 500MPa in magnitude [29]. Foreign object damage modifies this field to create a compressive peak of around 600MPa immediately below the impact. High Energy Synchrotron X-ray diffraction has been used to evaluate the evolution of the residual stress field surrounding the

FOD location for specimens that have been fatigued so as to grow cracks under LCF and combined HCF+LCF representative of aeroengine load cycles.

1. No significant relaxation has been observed after N = 1 or N = 100 blocks of combined cycle fatigue at S_{max} = 435 MPa (= 0.5 σ_y) prior to the nucleation of a crack

2. No significant relaxation in the peak compressive residual strain has been observed due to crack growth under CCF or LCF until very long cracks were observed.

3. Our evidence points to forward and reverse plastic zone sizes that are very small (<100 μm). This is the result of the superposition of compressive residual stresses upon the tensile fatigue cycles. These crack-tip plastic zones are too small to significantly reduce the misfits that lie at the heart of the LSP+FOD residual stress fields and so the cracks do not significantly relax the residual stress field until the tensile region of the stress field is reached at a depth of 6 mm below the leading edge.

4. This work suggests that linear elastic fracture mechanics approaches would be appropriate for the study of the fatigue behaviour because the effect of crack-tip plasticity is negligible from a residual stress or applied loading point of view.

6 Acknowledgements

The authors acknowledge Engineering and Physical Sciences Research Council (EPSRC) and the MOD Joint Grants Scheme for financial support (EP/E05658X/1), QinetiQ, and Rolls Royce plc for providing the materials, specimens and LSP treatment. The authors would like to thank the Advanced Photon Source (APS), Argonne National Laboratory, in Chicago, USA; ID-31, ESRF and HEMS, PETRA III for provision of synchrotron X-ray radiation facilities; and J D. Almer, Dr A. Fitch and Dr N. Schell for experimental assistance during the experiments and Prof. M Fitzpatrick for support and helpful discussions. Thanks are also due to co-workers at Portsmouth for the sample preparation and their valuable discussions. SZ is also grateful for funding from the Lloyd's Register Foundation (LRF), a UK registered charity and sole shareholder of Lloyd's Register Group Ltd, that invests in science, engineering and technology for public benefit, worldwide.

7 References

1. Tan Y, Wu G, Yang JM, Pan T. Laser shock peening on fatigue crack growth behaviour of aluminium alloy. Fatigue & Fracture of Engineering Materials & Structures. 2004;27(8):649-56.
2. Hatamleh O, Lyons J, Forman R. Laser and shot peening effects on fatigue crack growth in friction stir welded 7075-T7351 aluminum alloy joints. International Journal of Fatigue. 2007;29(3):421-34.
3. Rubio-Gonz·lez C, OcaÒa JL, Gomez-Rosas G, Molpeceres C, Paredes M, Banderas A, et al. Effect of laser shock processing on fatigue crack growth and fracture toughness of 6061-T6 aluminum alloy. Materials Science and Engineering A. 2004;386(1-2):291-5.
4. Yang JM, Her YC, Han N, Clauer A. Laser shock peening on fatigue behavior of 2024-T3 Al alloy with fastener holes and stopholes. Materials Science and Engineering: A. 2001;298(1-2):296-9.
5. Nalla RK, Altenberger I, Noster U, Liu GY, Scholtes B, Ritchie RO. On the influence of mechanical surface treatments--deep rolling and laser shock

peening--on the fatigue behavior of Ti-6Al-4V at ambient and elevated temperatures. Materials Science and Engineering A. 2003;355(1-2):216-30.
6. Ruschau JJ, John R, Thompson SR, Nicholas T. Fatigue crack nucleation and growth rate behavior of laser shock peened titanium. International Journal of Fatigue. 1999;21:199-209.
7. Shepard M, Smith P, Amer M. Introduction of compressive residual stresses in Ti-6Al-4V simulated airfoils via laser shock processing. Journal of Materials Engineering and Performance. 2001;10(6):670-8.
8. Zhang XC, Zhang YK, Lu JZ, Xuan FZ, Wang ZD, Tu ST. Improvement of fatigue life of Ti-6Al-4V alloy by laser shock peening. Materials Science and Engineering: A. 2010;527(15):3411-5.
9. King A, Steuwer A, Woodward C, Withers PJ. Effects of fatigue and fretting on residual stresses introduced by laser shock peening. Materials Science and Engineering: A. 2006;435-436:12-8.
10. Smith PR, Shepard MJ, Prevèy PS, and Clauer A. Effect of power density and pulse repetition on laser shock peening of Ti-6Al-4V. . Journal of Materials Engineering and Performance 2000;9:33-7.
11. Zabeen S, Preuss M, Withers PJ. Synchrotron Strain Mapping of the Residual Strain Distribution around Foreign Object Damage in Laser Shock Peened Ti-6AL-4V Alloy. Materials Science Forum. 2010;652(0):19-24.
12. Montross CS, Wei T, Ye L, Clark G, Mai Y-W. Laser shock processing and its effects on microstructure and properties of metal alloys: a review. International Journal of Fatigue. 2002;24(10):1021-36.
13. Farrahi GH, Lebrijn JL, Couratin D. Effect of shot peening on residual stress and fatigue life of a spring steel. Fatigue & Fracture of Engineering Materials & Structures. 1995;18(2):211-20.
14. Kim J-C, Cheong S-K, Noguchi H. Residual stress relaxation and low- and high-cycle fatigue behavior of shot-peened medium-carbon steel. International Journal of Fatigue. 2013;56(0):114-22.
15. Kim J-C, Cheong S-K, Noguchi H. Evolution of residual stress redistribution associated with localized surface microcracking in shot-peened medium-carbon steel during fatigue test. International Journal of Fatigue. 2013 ;55(0):147-57.
16. Torres MAS, Voorwald HJC. An evaluation of shot peening, residual stress and stress relaxation on the fatigue life of AISI 4340 steel. International Journal of Fatigue. 2002;24(8):877-86.
17. Zhuang WZ, Halford GR. Investigation of residual stress relaxation under cyclic load. International Journal of Fatigue. 2001;23, (0):31-7.
18. Buchanan DJ, John R. Relaxation of shot-peened residual stresses under creep loading. Scripta Materialia. 2008;59(3):286-9.
19. Dalaei K, Karlsson B, Svensson LE. Stability of shot peening induced residual stresses and their influence on fatigue lifetime. Materials Science and Engineering: A. 2011;528(3):1008-15.
20. John R, Buchanan DJ, Caton MJ, Jha SK. Stability of shot peen residual stresses in IN100 subjected to creep and fatigue loading. Procedia Engineering. 2010;2(1):1887-93.

21. John R, Buchanan DJ, Jha SK, Larsen JM. Stability of shot-peen residual stresses in an α+β titanium alloy. Scripta Materialia. 2009 ;61(4):343-6.
22. Schulze V. Changes of Surface Layer States due to Quasi-static Loading. Modern Mechanical Surface Treatment: Wiley-VCH Verlag GmbH & Co. KGaA; 2005. p. 179-245.
23. Schulze V. Changes of Surface States during Cyclic Loading. Modern Mechanical Surface Treatment: Wiley-VCH Verlag GmbH & Co. KGaA; 2005. p. 247-353.
24. Hall R, Byrne J, Zhao T, Tong J. Influence of foreign object damage on fatigue crack growth of gas turbine aerofoils under complex loading conditions. Fatigue and Fracture of Engineering Materials and Structures. 2008;31(5):386-97.
25. Frankel PG, Withers PJ, Preuss M, Wang H-T, Tong J, Rugg D. Residual stress fields after FOD impact on flat and aerofoil-shaped leading edges. Mechanics of Materials. 2012;55:130-5.
26. Thompson SR, Ruschau JJ, Nicholas T. Influence of residual stresses on high cycle fatigue strength of Ti-6Al-4V subjected to foreign object damage. International Journal of Fatigue. 2001;23:405-12.
27. Boyce BL, Chen X, Hutchinson JW, Ritchie RO. The residual stress state due to a spherical hard-body impact. Mechanics of Materials. 2001;33(420):441-54.
28. Hammersley G, Hackel LA, Harris F. Surface prestressing to improve fatigue strength of components by laser shot peening. Optics and Lasers in Engineering. 2000;34(4-6):327-37.
29. Zabeen S, Preuss M, Withers PJ. Residual stresses caused by head-on and 45° foreign object damage for a laser shock peened Ti–6Al–4V alloy aerofoil. Materials Science and Engineering: A. 2013 ;560(0):518-27.
30. Ding J, Hall RF, Byrne J, Tong J. Fatigue crack growth from foreign object damage under combined low and high cycle loading. Part II: A two-parameter predictive approach. International Journal of Fatigue. 2007;29(7):1350-8.
31. Nowell D, DuÛ P, Stewart IF. Prediction of fatigue performance in gas turbine blades after foreign object damage. International Journal of Fatigue. 2003 ;25(9-11):963-9.
32. Spanrad S, Tong J. Characterisation of foreign object damage (FOD) and early fatigue crack growth in laser shock peened Ti-6Al-4V aerofoil specimens. Materials Science and Engineering: A. 2011;528(4-5):2128-36.
33. Zabeen S. Fatigue crack growth in complex residual stress fields due to surface treatment and foreign object damage under simulated flight cycles. Manchester: The University of Manchester; 2012.
34. Withers PJ. Synchrotron X-ray Diffraction. Practical Residual Stress Measurement Methods: John Wiley & Sons, Ltd; 2013. p. 163-94.
35. Owen A. Synchrotron strain mapping: Aerospace applications

Manchester: University of Manchester; 2002.
36. Daymond MR, Bonner NW. Lattice strain evolution in IMI 834 under applied stress. Materials Science and Engineering A. 2003;340(1-2):272-80.

37. Withers PJ, Preuss M, Steuwer A, Pang JWL. Methods for obtaining the strain-free lattice parameter when using diffraction to determine residual stress. Journal of Applied Crystallography. 2007;40(5):891-904.
38. Boyce BL, Chen X, Peters JO, Hutchinson JW, Ritchie RO. Mechanical relaxation of localized residual stresses associated with foreign object damage. Materials Science and Engineering A. 2003;349(1-2):48-58.
39. Withers PJ. Residual stress and its role in failure. Reports on Progress in Physics. 2007;70:2211–64.
40. Dias A, Lebrun JL, Bignonnet A. X-ray diffraction studies on fatigue crack plastic zones developed under plane strain state conditions. Fatigue & Fracture of Engineering Materials & Structures. 1999 Feb;22(2):133-44. PubMed PMID: ISI:000080123900005.
41. Withers PJ. Fracture Mechanics by 3D Crack-tip Synchrotron X-ray Microscopy. Phil Trans R Soc A. 2014:Accepted for Publication.
42. Rice JR. Mechanics of crack tip deformation and extension by fatigue. Fatigue Crack Propagation: ASTM STP 415; 1967. p. 247-309.
43. McClung RC. Craack closure and plastic zone sizes in fatigue Fatigue & Fracture of Engineering Materials & Structures. 1991;14(4):455-68.

8 Figures

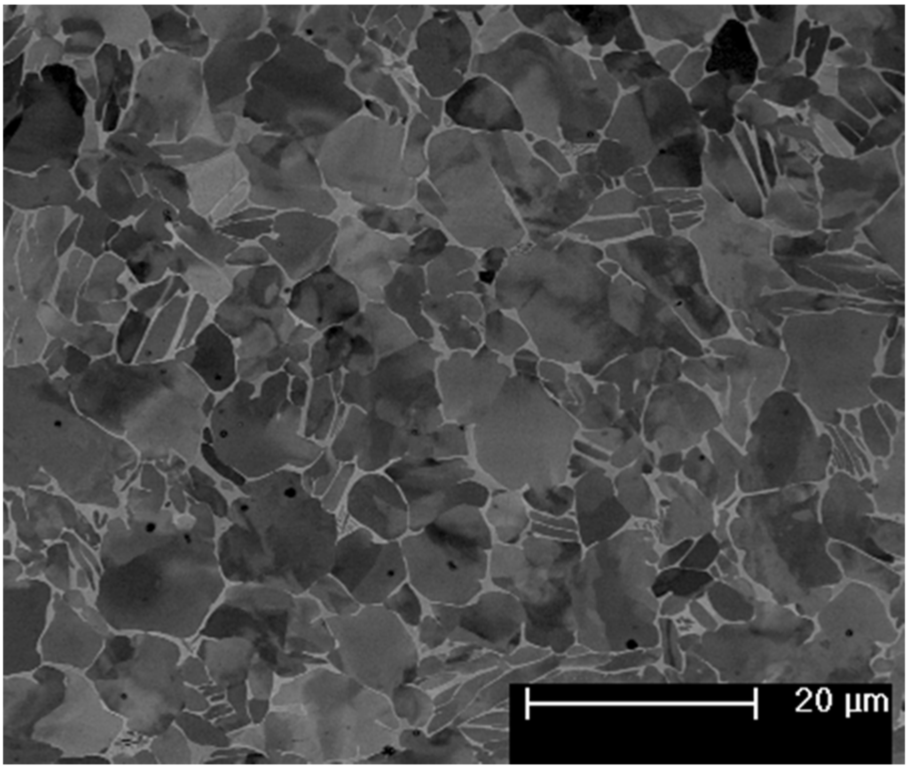

Figure 1: Scanning electron micrograph of the as-received microstructure of Ti-6Al-4V.

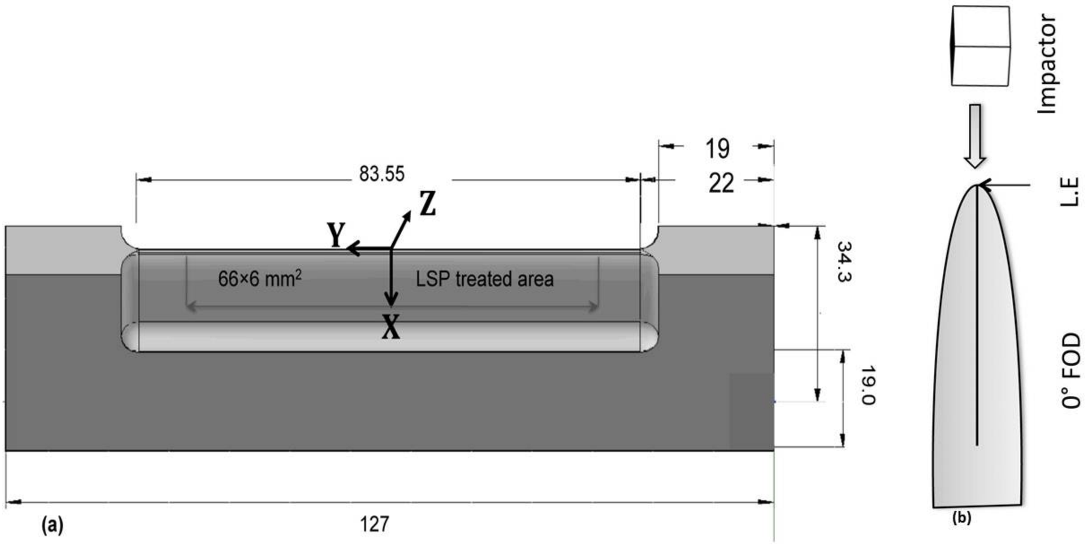

Figure 2: a) Laser shock peened four-point bend (4PB) simulated aerofoil specimen geometry (all dimensions are given in mm) including a description of the coordinate system with (0,0,0) at the centre of the leading edge, b) Schematic representation of the Head-on (0°) FOD impact configuration.

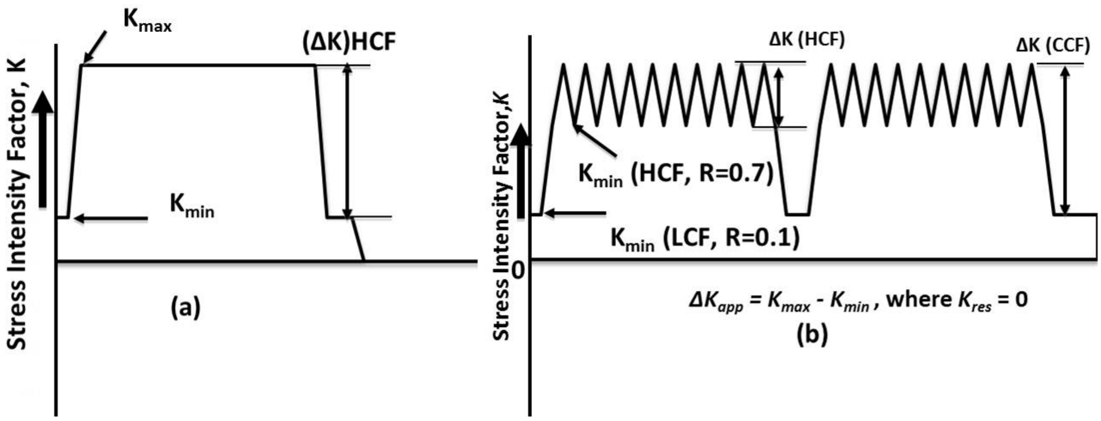

Figure 3: Schematic representation of (a) LCF and (b) combined fatigue cycles (CCF=1000 HCF cycles superimposed onto 1 LCF cycles).

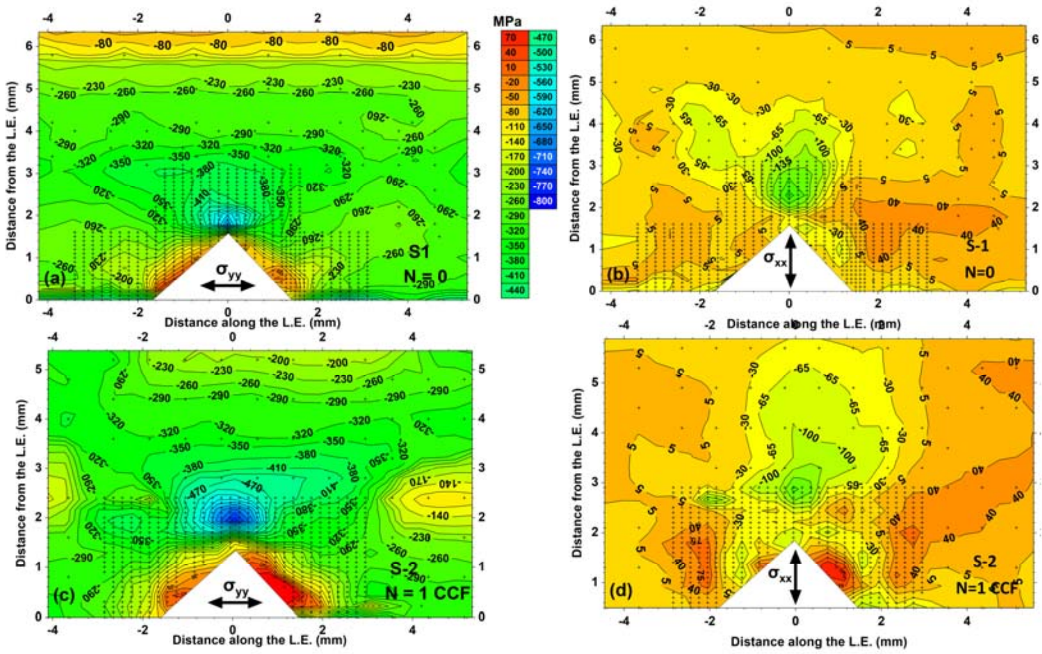

Figure 4: Residual elastic stress parallel (left) and perpendicular(right) to the leading edge around a FOD impact a) prior (S-1) and b) subsequent to (S-2) 1 combined fatigue cycle (CCF=LCF+1000HCF, S_{max}=435 MPa and R_{LCF} = 0.1 and R_{HCF} =0.7). The notch depth for this sample (S-2) is 1.55mm. Measurement locations are indicated by (+). The error in results lies within ±20 MPa.

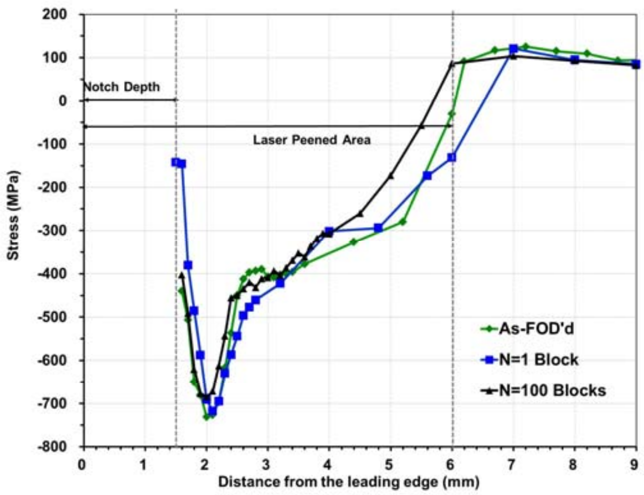

Figure 5: Comparison of residual elastic strain profiles along the line of the notch (y=0) for a 0° FOD impact after 0 (S-1), 1(S-2) and 100 (S-2) blocks of combined cycle fatigue. The error in results lies within ±20 MPa.

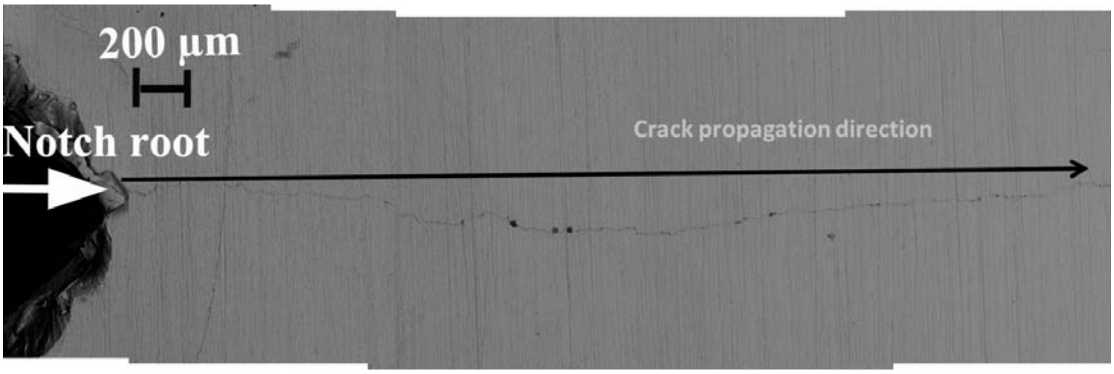

Figure 6: SEM micrograph of specimen (S-6) showing the site of crack initiation and the crack path (Δa=5.3mm).

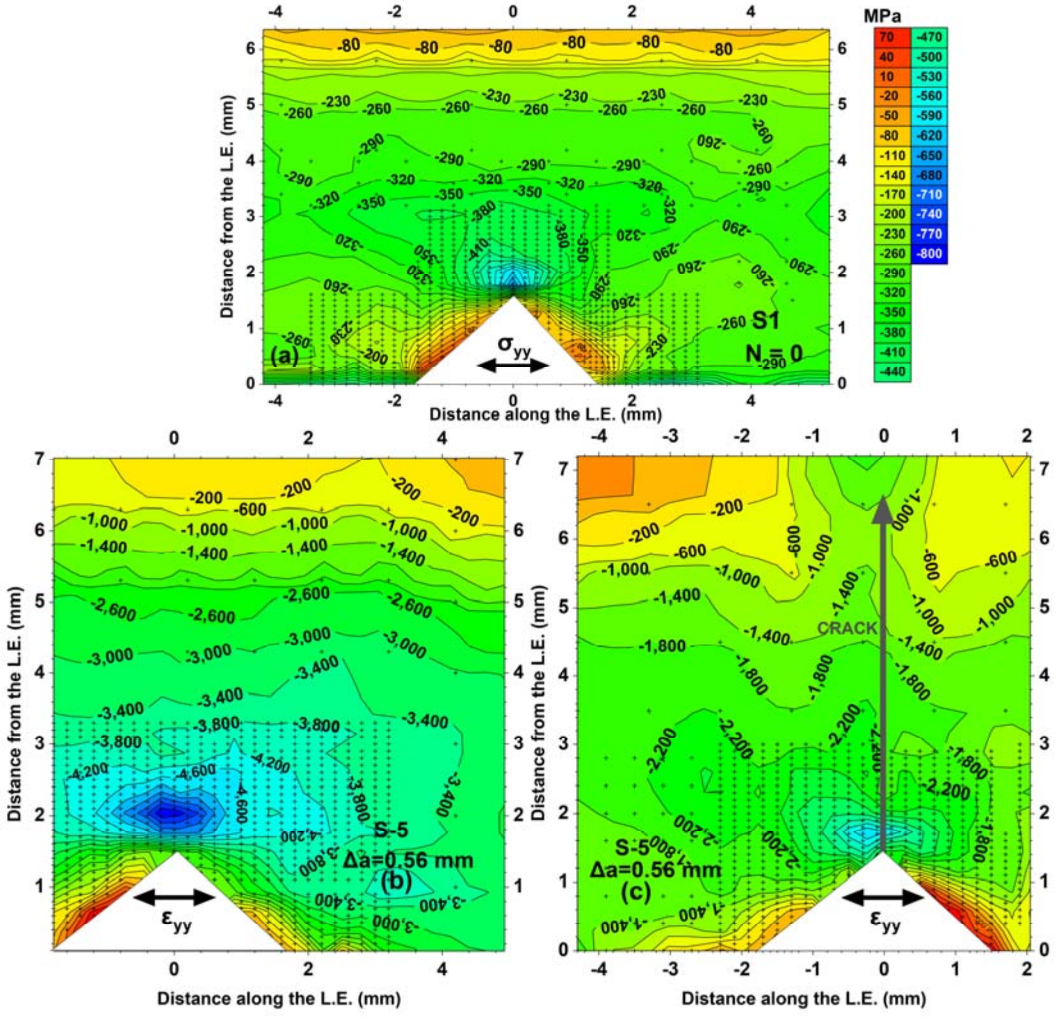

Figure 7: Through thickness averaged 2D residual strain (× 10^{-6}) map for LCF (S_{max}=586 MPa) as a function of crack growth (a) for Δa=0 (prior to LCF (S-1), The notch depth is 1.5 mm (b) for Δa = 0.56 mm (20,272 LCF cycles (S-5)) (c) for Δa = 5.3 mm (34300 LCF cycles (S-6)) The error in results lies within ±200 microstrains.

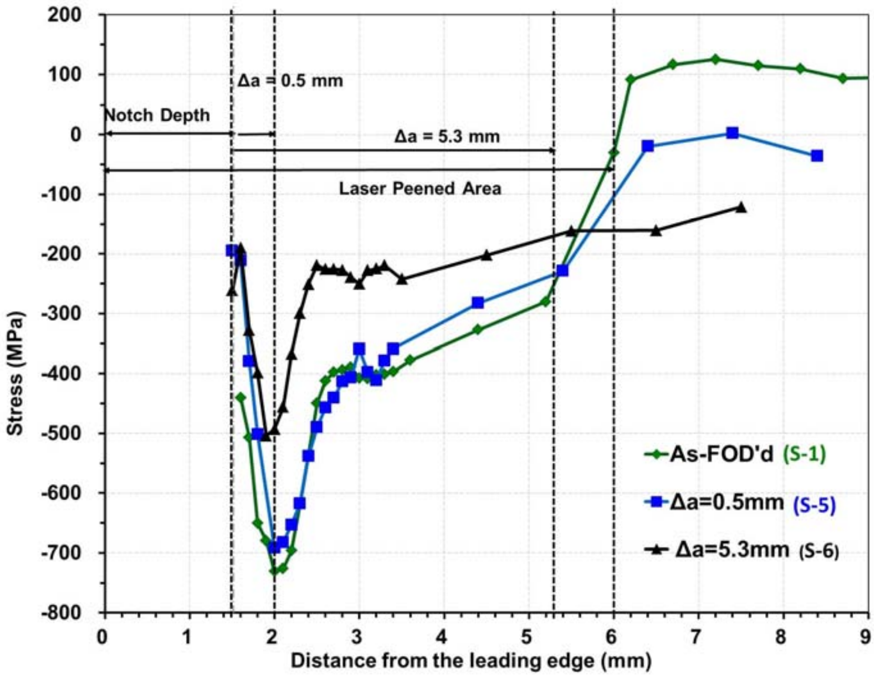

Figure 8: Comparison of residual elastic strain profiles along the line of the notch (y=0) for a 0° FOD impact after 0mm (S-1), 0.5mm (S-5) and 5.3mm (S-6) LCF fatigue crack growth.

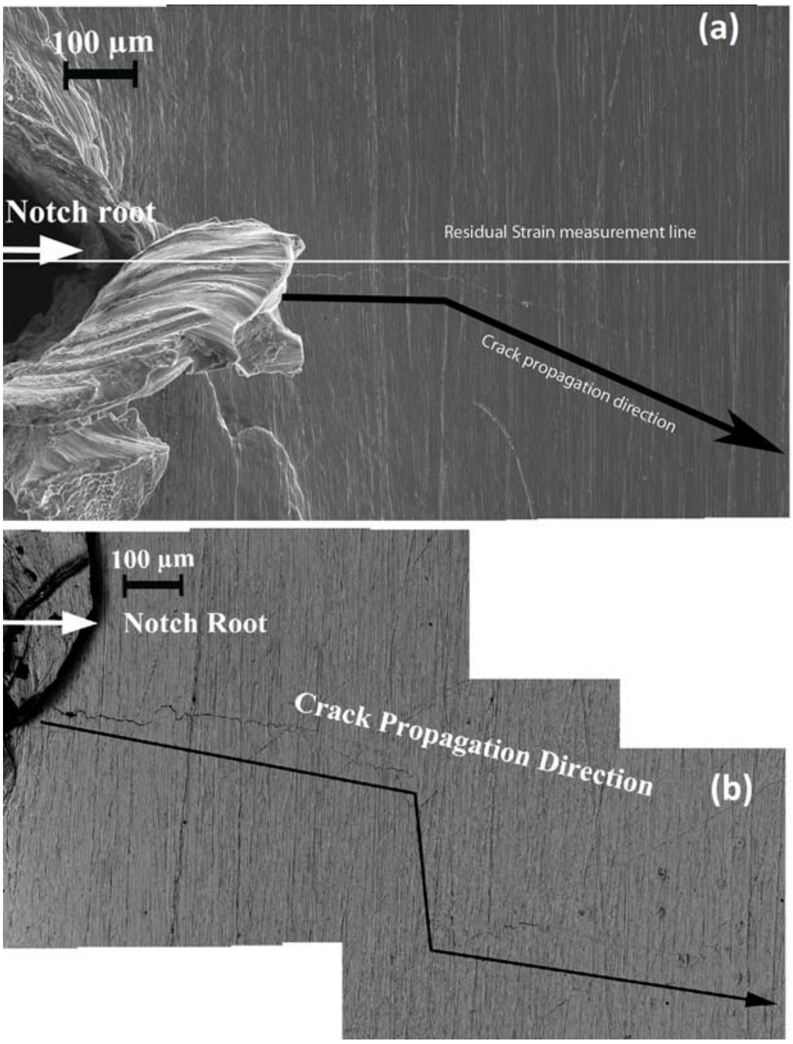

Figure 9: SEM images showing the crack initiation and propagation under LCF + HCF loading in 0° impacted specimens (a) for specimen S-2, and (b) S-3.

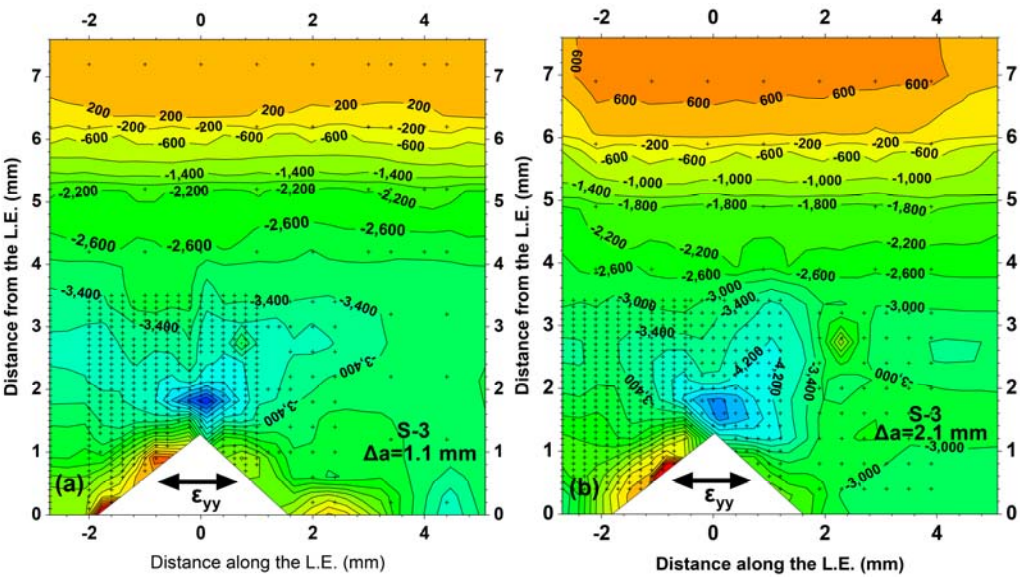

Figure 10: Through thickness averaged 2D residual strain map for 0° FOD impact: (a) crack length, Δa=1mm, N=2979 blocks and S_{max}=434MPa (S-3), (b) Δa =2.1mm N= 3400 blocks, applied stress of S_{max}=434MPa (S-3). The error in results lies within ±200 microstrains.

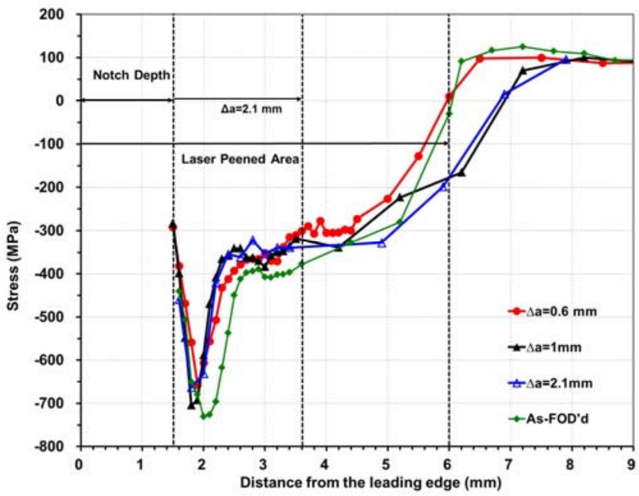

Figure 11: Comparison of residual strains prior to (Δa=0) and subsequent to combined cycle fatigue (S_{max} =343MPa) sufficient to grow a crack to Δa = 0.6 (2744 blocks), 1 (2979 blocks) and 2.1 mm (3400 blocks) (S-3).

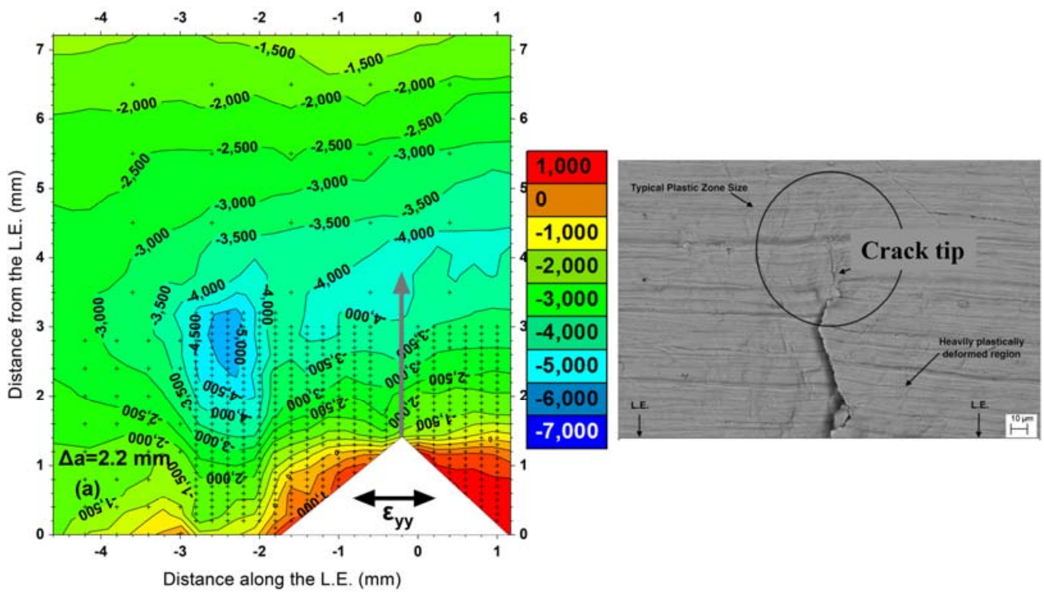

Figure 12: (a) Longitudinal residual strain distribution for overloaded specimen (S-4, S_{max}>860MPa) (The error in results lies within ±200 microstrains) and (b) SEM images of a 2.2 mm long crack.

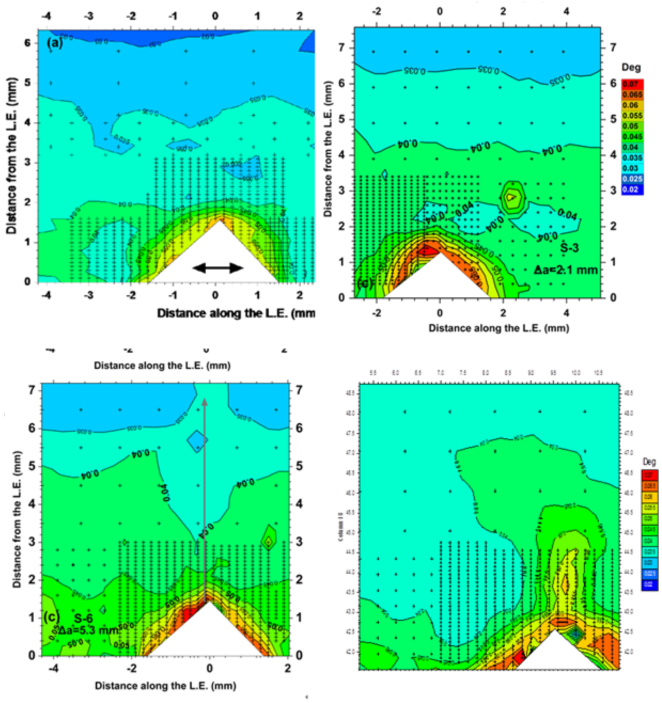

Figure 13: Maps of FWHM of $(10\bar{1}2)$ the (a) prior to fatigue cycling, (b) after 2.1 mm growth under CCF, (c) after 5.3 mm growth under LCF, and (d) after rapid crack growth under an overload.

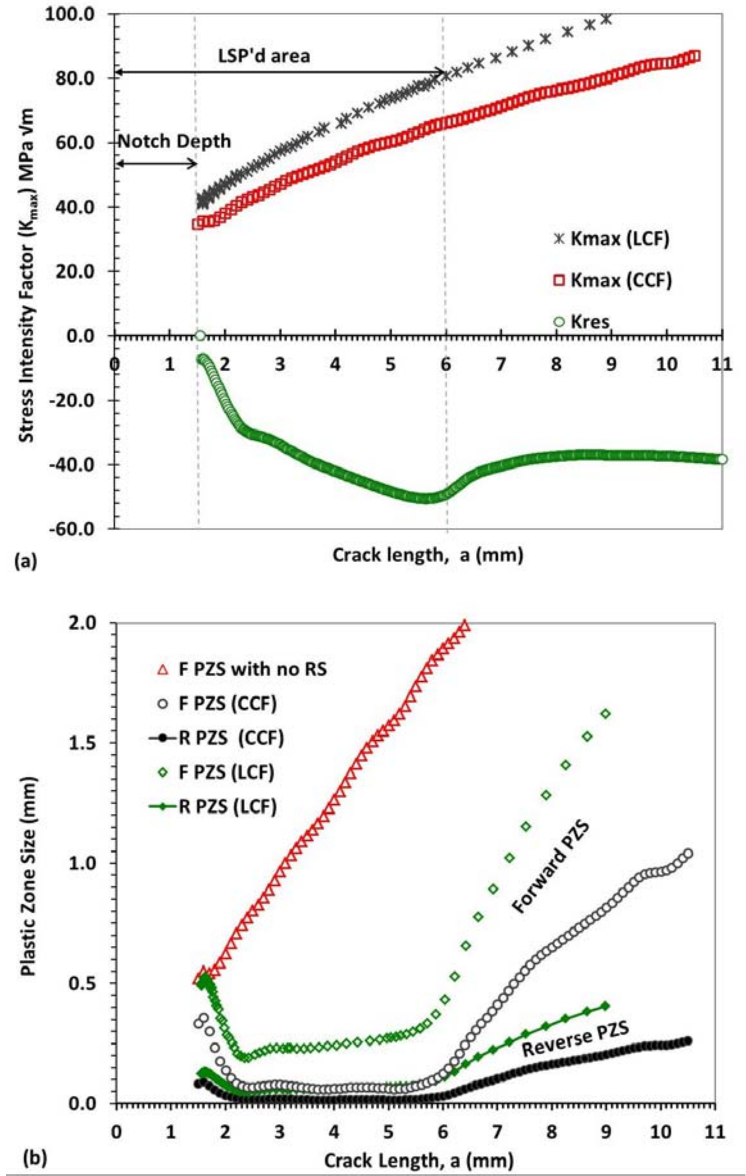

Figure 14: (a) Variation of K_{res} and estimated variation of K_{max} with crack length under CCF and LCF loading conditions without considering residual stress and (b) Forward and reverse plastic zone for both 0° impact, found using Equation 2 and 3 respectively for CCF loading condition at S_{max}=435 MPa for CCF and S_{max}=586 for the LCF condition.